Emergence of a Fermi surface in the current-driven hidden state of 1*T*-TaS_2

Yuval Nitzav,[1] Roni Anna Gofman Kiassi,[1] Ilay Mangel,[1] Abigail Dishi,[1] Nitzan Ragoler,[1] Sajilesh K. P.,[1] Yaron Jarach,[1] Alex Louat,[2] Matthew D. Watson,[2] Cephise Cacho,[2] Irena Feldman,[1] and Amit Kanigel[1,*]

[1]*Department of Physics, Technion, Haifa, 3200003, Israel*

[2]*Diamond Light Source, Harwell Science and Innovation Campus, Didcot OX11 0DE, United Kingdom*

(Received 17 April 2025; revised 5 November 2025; accepted 19 December 2025; published 3 February 2026)

The origin of the insulating state in 1*T*-TaS_2 has long been a subject of debate. A short current pulse transforms this insulating state into a metastable metallic phase. Using micro–angle-resolved photoemission spectroscopy, we investigate the electronic structure of this phase and uncover spatially dependent modifications caused by the current pulse. In some regions of the sample, a Fermi surface emerges, while others remain gapped. Detailed band structure analysis reveals that the metallic regions exhibit an electronic structure similar to that observed in the high-temperature phase of 1*T*-TaS_2, characterized by suppressed energy gaps and bands crossing the Fermi level. Furthermore, the metallic and insulating regions display distinct out of plane dispersions, consistent with the current pulse influencing the Star of David dimers that characterize the insulating phase.

DOI: 10.1103/kj9t-8mys

Metastable and hidden states have emerged as key areas of interest in condensed matter physics, offering insights into novel phases of matter and exotic physical properties. They also present promising avenues for technological applications. A metastable state occurs when a system becomes trapped in a local energy minimum rather than reaching its global ground state. These states typically arise from competing orders [1–3], topological defects [4], structural configurations [5], and other degrees of freedom that create a complex energy landscape with multiple stable configurations. Some metastable states can be accessed thermally, for example, by rapidly cooling a material from elevated temperatures [6,7]. Distinctly, hidden states represent a subset of metastable states that require nonthermal stimuli. These hidden configurations can only be reached through external drivers like ultrafast laser pulses or strong electric fields [8–11].

The study of these metastable states provides valuable insights into material properties and underlying physical mechanisms. By examining metastable configurations, we can better understand fundamental interactions in materials, for example, electron-phonon coupling [12] and magnetic-lattice interactions [9].

One such hidden phase is the metallic state induced at low temperatures in 1*T*-TaS_2 by various stimuli, including a short light pulse [13], charge transfer [14], or a short electric current pulse [15]. Regardless of the perturbation method, the hidden state exhibits a similar critical temperature [16] and relaxation timescales [17]. Following the short pulse, the resistance of the samples is reduced by up to several orders of magnitude. This hidden metallic state has been shown to persist for hours and is fully reversible when the sample is either heated above a certain temperature [17] or subjected to an erasing pulse [13].

Due to the fast and controllable nature of the transition to the hidden state [18], it has been suggested for various applications, including programmable light manipulation [19] and charge configuration memory (CCM) devices [15,16,20,21].

The origin of the insulating ground state exhibited by 1*T*-TaS_2 remains unknown. The electronic structure is governed by a charge density wave (CDW) instability [22,23]. The main motif of the CDW is a rearrangement of every 13 Ta atoms in a Star of David cluster where 12 Ta atoms are displaced towards the middle 13th atom. Below 352 K domains of Star of David supercells start to form. The domains are separated by regions with no CDW and form a hexagonal lattice which is nearly commensurate (NC) with the atomic lattice [24–26]. Below 183 K all the Star of David domains merge to create a commensurate CDW (CCDW) state. The CCDW vectors are rotated by $\pm 13.9^\circ$ from the atomic-lattice vectors and form a new $\sqrt{13} \times \sqrt{13}$ sized unit cell. The orientation of the CDW vectors breaks mirror symmetry, and gives rise to two degenerate configurations [see Fig. 4(e)] with a distinct chirality. The sample's chirality is established during the formation of the CDW domains in the NCCDW phase and persists into the CCDW state [27], where these chiral domains can extend to millimeter-scale sizes [28].

The phase transition from NCCDW to CCDW is marked by an abrupt increase in resistivity, followed by strong insulating behavior at lower temperatures. In the CCDW state, the valence band splits into seven narrow bands, six of which are fully occupied, while the topmost band is half filled. The presence of unpaired electrons suggests that the CCDW alone cannot fully explain the observed insulating state [29,30].

It has been proposed that the narrow half-filled band in 1*T*-TaS_2 undergoes a Mott transition to an insulating state [31,32]. In recent years, it has become evident that the out of plane stacking of Star of David clusters plays a significant role in determining the electronic properties of 1*T*-TaS_2 [33,34]. Evidence for out of plane dimerization is observed during the transition to the CCDW state [35], resulting in an even number of electrons per unit cell and leading to insulating behavior

*Contact author: kanigel.amit@gmail.com

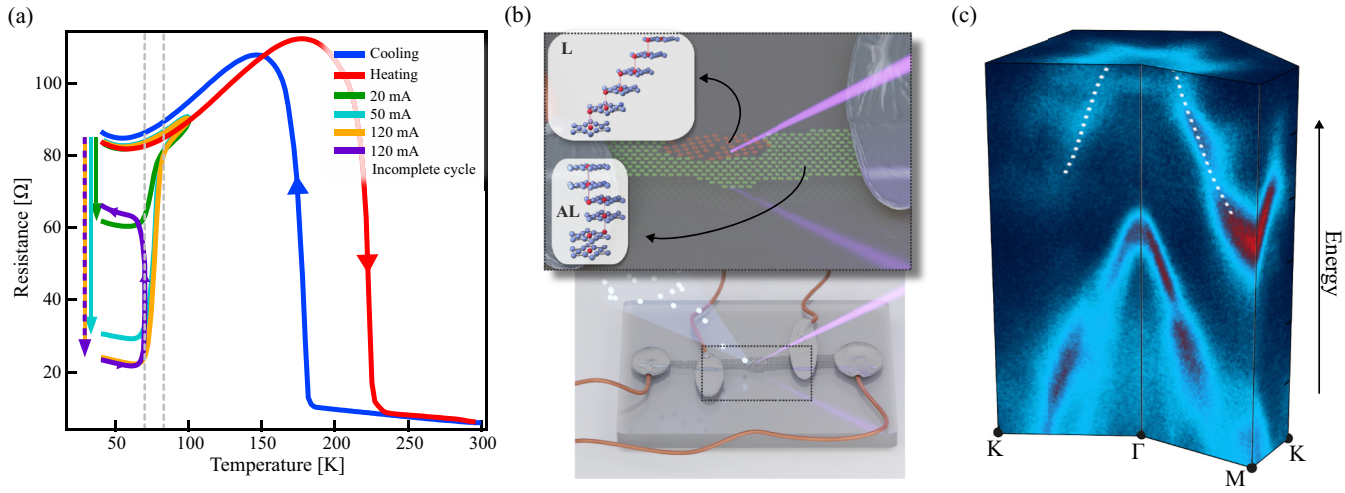

FIG. 1. The hidden metastable state in 1*T*-TaS_2. (a) Resistance as a function of temperature for a typical sample used in the ARPES experiment. The blue and red curves represent the sample resistance during cooling and heating, respectively, without any perturbation. The green, cyan, and orange curves illustrate the reduction in resistance with the application of progressively larger current pulses. The purple curve shows an incomplete recovery to the "normal" state after the application of a 120 mA pulse. (b) Schematic illustration of the micro-ARPES experiment. A thin 1*T*-TaS_2 sample is fixed to a sapphire substrate using Ag epoxy. Four contacts are used to apply current and measure the voltage across the sample. A micron-sized beam spot is employed to scan the electronic spectrum of the device. In the hidden state, the sample is phase separated into metallic and insulating areas. The out of plane dispersion reveals that the unit cell in the insulating regions is twice as large as that in the metallic regions, which is consistent with AL stacking and L stacking, respectively [34]. (c) ARPES data from the metallic part along high-symmetry lines. Following the current pulse, a Fermi surface emerges in parts of the sample. The dispersion of the NCCDW at 300 K is indicated by the dotted white line.

[36]. Scanning tunneling microscopy (STM) measurements reveal that the monolayer 1*T*-TaS_2 is insulating [37], consistent with Mott insulating behavior in the absence of interlayer coupling. However, it remains unclear whether this behavior persists in the bulk, where out of plane interactions play a critical role. Understanding the nature of the metallic hidden state may provide insights into the origin of the insulating ground state.

In this paper, we use spatially resolved angle-resolved photoemission spectroscopy (ARPES) to track the evolution of the electronic structure of 1*T*-TaS_2 after a short current pulse. Our main results are summarized in Fig. 1. Following a short current pulse, the resistance of the sample at low temperatures decreases by a factor of about 4 [Fig. 1(a)]. In this state, we observe a nonuniform electronic structure, with different parts of the sample exhibiting distinct behaviors [Fig. 1(b)]. Most of the sample remains in the CCDW state, characterized by a full gap and a clear band folding due to the CDW, both in plane and out of plane. However, other regions, which contribute to the enhanced conductance in the hidden state, display a much weaker CDW effect and have a clear Fermi surface [Fig. 1(c)]. The ARPES spectrum in these parts has some similarities with the NCCDW spectrum although STM measurements find a completely different domain morphology in the two states [4].

I. MATERIALS AND METHODS

A. Sample preparation

The 1*T*-TaS_2 single crystals were grown as described in Ref. [38]. Samples of 1*T*-TaS_2 were prepared for nano-ARPES experiments: Single crystals were cut into narrow bridges 200−500 μm in width. The samples were glued to a sapphire substrate and four contacts were made using Ag epoxy. The samples were cooled to 40 K and cleaved under UHV conditions. The four contacts were used to drive a current pulse and to monitor the sample resistance *in situ*. We emphasize that during the ARPES measurement no current was applied to the sample. The ARPES and transport measurements in this work were performed on devices from different samples and crystal growth batches. All samples exhibited the same qualitative transition and behavior, demonstrating that the observed phenomena are not specific to a particular device. Minor variations in resistance values and transition thresholds are expected from differences in sample dimensions and contact geometry.

B. ARPES measurements

Spatially resolved ARPES experiments were carried out in the I05 beamline at Diamond Light Source, UK. The spatial resolution is set by the beam spot size, which in our experiment was either 500 nm using a zone plate or 5 μm using a capillary mirror. Energy resolution was set to about 50 meV. Data in the NCCDW state were measured at the CASSIOPEE beamline at Soleil, France. Measurements were done at room temperature using 80 eV photon energy. Beam spot size was 100 μm. Energy resolution was set to 20 meV. The Fermi level was determined by measuring a metallic sample at the same conditions.

II. RESULTS

A. Transition to the hidden state

In Fig. 1(a), we present the resistance as a function of temperature for a typical bridge. An abrupt change in resistance is

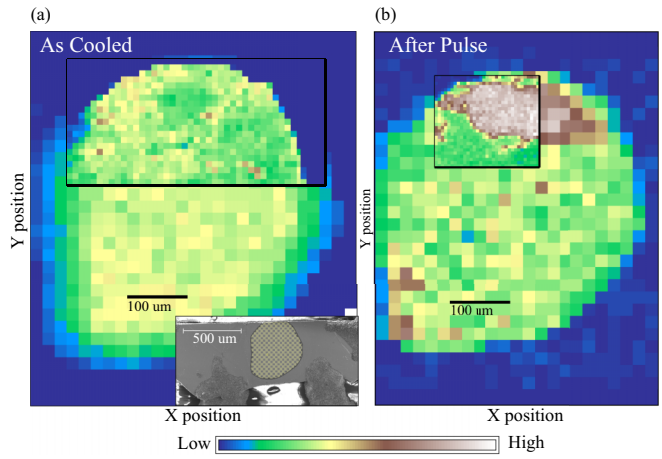

FIG. 2. Maps of the spectral weight at the Fermi level. Micro-ARPES maps were measured with a spot size of 5 microns at 40 K. The step size was set to 20 microns, and was reduced in the area marked by a solid black line to 10 microns in (a) and 5 microns in (b). The color map represents the integrated ARPES intensity at the Fermi level. In (a), we show the sample in the CCDW state. The sample was first driven into the hidden state [shown in (b)], and then was removed from the cryomanipulator to be warmed and cooled back down to 40 K. The entire scan shows low intensity, indicating a gapped state. The inset is a SEM image showing the sample with Ag epoxy contacts, with the cleaved area marked on the image. In (b), we show a spatial scan after a 190 mA current pulse. High-intensity regions can be seen. In these areas, the gap is closed, and we observe a metallic Fermi-Dirac edge.

observed when cooling into the CCDW state at approximately 180 K (blue line) and when warming back up at approximately 220 K (red line).

At a temperature of 40 K, a current pulse was applied, drastically lowering the sample's resistance. This low resistance is maintained as long as the temperature remains below 70 K, which is consistent with the transition temperature observed when a short light pulse was used to drive the transition [17].

As higher current pulses are applied, the sample's resistance decreases further, eventually saturating at around 140–190 mA for our typical sample dimensions. Upon warming, the resistance returns to its initial value. If the sample is cooled before a complete transition back to the CCDW phase, it becomes locked in an intermediate state [see the purple line in Fig. 1(a)].

B. Spatial distribution of the hidden state

In Fig. 2 we show maps of the spectral weight at the Fermi level over the entire cleaved area measured at 40 K, before the current pulse [Fig. 2(a)] and after the current pulse [Fig. 2(b)]. The color map represents the momentum-integrated intensity of the micro-ARPES spectra at the Fermi level. The spatial resolution is set by the spot size which is about 5 microns in this case. The inset of Fig. 2(a) shows a scanning electron microsope (SEM) image of the measured sample. The cleaved area is marked.

Before the pulse, in the CCDW state, we observe a small, spatially uniform spectral weight at the Fermi level, originating from the tail of the flat band located at a binding energy of approximately 100 meV. Following the current pulse, we find regions of high intensity indicating metallic parts of the sample where the spectral gap is closed. The emergence of the metallic parts is fully reversible; in fact, the data in Fig. 2(a) were measured after the data in Fig. 2(b) by warming the sample and cooling it down again, restoring the CCDW phase.

The use of a current pulse to drive the transition results in an inherently inhomogeneous state. Unlike a laser pulse, the current flow profile between the contacts cannot be precisely controlled and is generally nonuniform. Consequently, it is reasonable to assume that metallic regions form where the current density is sufficiently high. After the pulse, the sample is therefore phase separated into metallic regions and regions that remain in the CCDW insulating state. This inhomogeneity is not a characteristic of the hidden state but rather specific to the sample.

We observed different patterns of phase separation in the samples we measured and were unable to find defects on the sample surface that pin the metallic parts in the hidden state, suggesting that the switching is governed by the bulk current flow profile. Recently, it has been suggested that the metallic areas are more likely to form at the sample boundary [40].

C. Band dispersion of the hidden state

Next, we follow the evolution of the spectra at one point in the sample that becomes metallic upon the application of the current pulse. In Fig. 3, we present typical micro-ARPES data along the Γ-M direction, measured using 80 eV photon energy and a submicron spot size. Figure 3(a) shows the timeline of the experiment. First, the sample was cooled to 40 K. The data before any current pulse was applied are shown in Fig. 3(b), revealing the signature CCDW gaps and a flat band around the Γ point. A 140 mA, 1 ms long pulse was then applied, reducing the resistance by a factor of 4. Figure 3(c) presents the ARPES data after the current pulse, showing a suppression of the CDW gaps and a band crossing the Fermi level at $k_F = \pm 0.4\,\text{Å}^{-1}$. The intensity of the flat band at the Γ point is significantly suppressed. The sample was then removed from the cryomanipulator and allowed to warm up in the vacuum chamber for approximately 10 min before being cooled back to base temperature. Following this thermal cycle, the resistance partially recovered to about half of the original value. It is important to note that the exact temperature during this warm-up sequence is unknown. The data in Fig. 3(d) show developed CCDW gaps and a partial recovery of the flat band. A second current pulse was then applied and the resistance dropped to a tenth of the original resistance. Figure 3(e) shows ARPES data after the second current pulse. Again, the CCDW gaps are closed and a metallic band is formed. For comparison, we show by the white dashed line the band dispersion measured at room temperature, in the NCCDW state, using a ~100 micron spot size. The agreement with the hidden state dispersion is remarkable.

In Figs. 3(f)–3(h) we show energy distribution curves (EDCs) at $k = 0$ [Fig. 3(f)], $k = 0.32\,\text{Å}^{-1}$ [Fig. 3(g)], and at $k_F = 0.44\,\text{Å}^{-1}$ [Fig. 3(h)], showing the flat band and the CCDW gaps. At the Γ point [Fig. 3(f)] we can see a suppression of the flat band in the hidden state. The band does

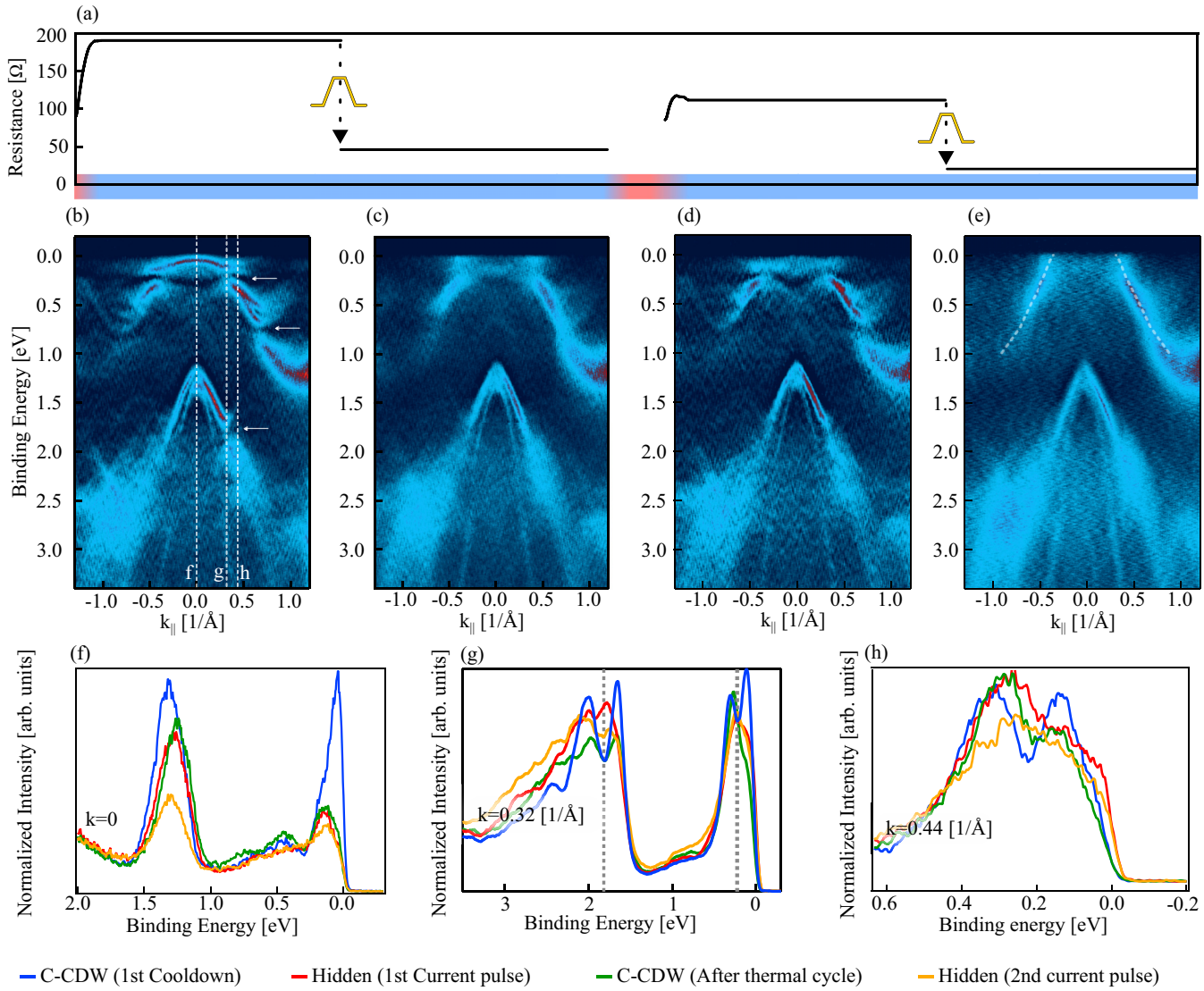

FIG. 3. ARPES spectra in the hidden state. Micro-ARPES spectra at 40 K, measured with 80 eV photons along the Γ-*M* direction. (a) Experimental timeline, showing the sample's resistance plotted as a function of time. The color bar represents the temperature of the sample over time. (b) ARPES image after the initial cooldown, in the CCDW state. The resistance of the sample at this stage is ∼200 Ω. One can see the characteristic flat band at Γ and the CDW gaps marked by white arrows. The dashed white lines indicate the momenta at which the EDCs are displayed in panels (f)–(h). (c) The spectra after a 140 mA, 1 ms long current pulse; the resistance dropped to 46 Ω. The CDW is highly suppressed, as evidenced by the suppressed band folding and CDW gaps. The band is crossing the Fermi level at $k_{\parallel} = 0.44$ Å^{-1}. (d) ARPES image after the sample was removed from the manipulator, allowed to warm up, and then reinserted and cooled down. The sample resistance is 115 Ω, not fully restored. The CDW gaps are partially recovered. (e) ARPES image after a second, 140 mA pulse was applied. The resistance dropped to 20 Ω. Again, the flat band and the CDW gaps vanish. The dashed white line shows the dispersion in the NCCDW state measured at room temperature using standard ARPES. The measurements in (b)–(d) were all measured at approximately the same position on the sample. (f) EDCs at the Γ point. The flat band is suppressed by the pulses and only partially recovered in (c). The folded band due to the CCDW is visible as a peak at −450 meV in the CCDW state (green, blue) while absent in the hidden state (red, orange). (g) EDCs at $k = 0.32$ Å^{-1}. Gray dotted lines show the CCDW gap position. The gap is clear in the CCDW state (blue, green) and it is strongly suppressed in the hidden state (red, orange). (h) EDCs taken at $k_F = 0.44$ Å^{-1} show a metallic Fermi edge for the EDCs measured in the hidden state (red, orange).

not fully recover after the thermal cycle. The small peak at $\simeq -0.45$ eV is a signature of the folded band due to the CCDW and is absent in the hidden phase. In Fig. 3(g) we find well developed gaps in the EDCs that correspond to the CCDW state (marked with gray dashed lines), and a suppression of the gap in the EDCs measured in the hidden state. In Fig. 3(h) we show a metallic Fermi edge in the EDCs taken in the hidden state and a gap at the Fermi level for EDCs in the CCDW state. The same behavior was observed in several different locations on the sample.

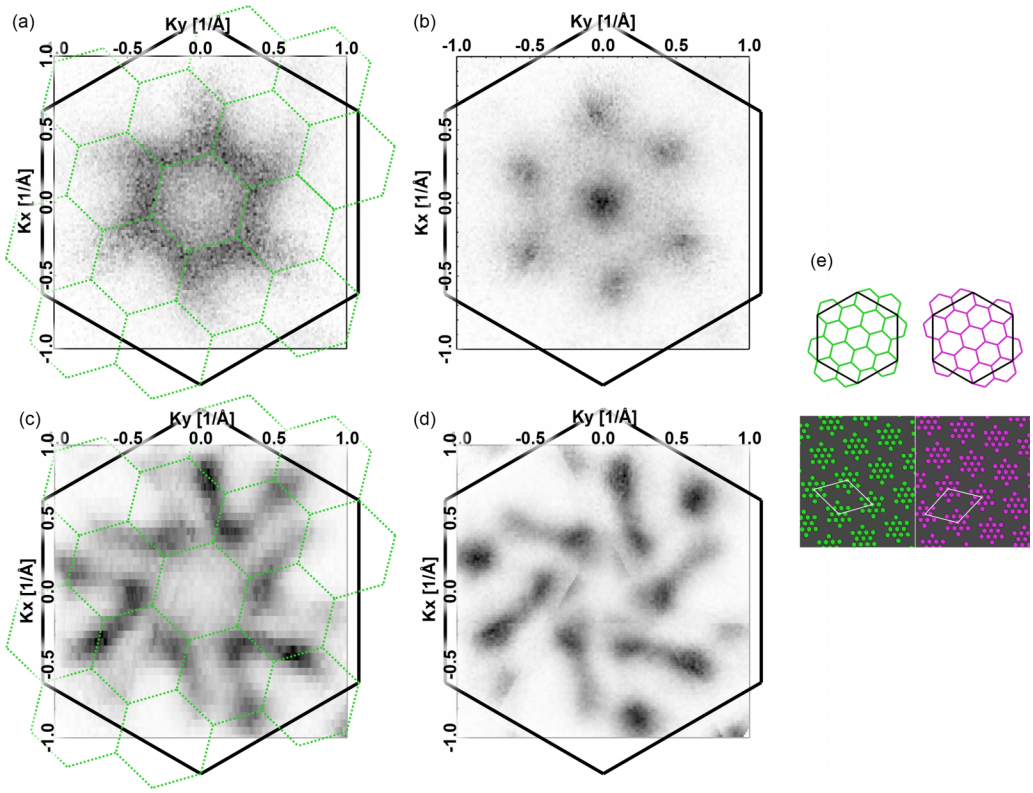

FIG. 4. ARPES intensity maps. Constant energy maps at metallic and insulating regions, following a current pulse. Data measured using 80 eV photon energy. The maps are generated by rotating the measured region by 120° to reconstruct the full Brillouin zone. The large hexagon (solid black line) represents the normal state Brillouin zone (BZ). Small hexagons in green are the CDW reconstructed BZs. (a) Fermi surface obtained from a metallic region by averaging the spectral weight within ±10 meV of the Fermi level. (b) Constant energy map from an insulating region, measured at a binding energy of 30 ± 5 meV. (c),(d) Constant energy maps measured at 300 ± 5 meV in the metallic and insulating parts, respectively. Both show a distinct chirality which originates from the formation of the Star of David clusters. We find the same chirality in the metallic and insulating regions. (e) The two possible mirror symmetry breaking CCDW configurations. Top: BZ of each configuration resulting from the real-space CCDW configuration illustrated below.

D. Chirality of the Fermi surface

ARPES intensity maps measured following the current pulse at two different locations on the sample, one in a metallic region and the other in an insulating region are shown in Fig. 4. In the metallic part, at the Fermi level, we find a clear Fermi surface (FS) [Fig. 4(a)]. This FS is the origin of the enhanced conductivity in the hidden state. The FS is similar to the FS found in the high-temperature NCCDW state [41]. It consists of six elliptical pockets centered around the *M* points. The Fermi pockets are gapped near the Brillouin zone (BZ) edges, resulting in an incomplete Fermi surface [23,42].

In the insulating regions, there is no Fermi surface, but we observe intensity at low binding energies extending almost to the Fermi level. Figure 4(b) shows an intensity map at a binding energy of 30 meV. We find some spectral weight at the Γ point of the atomic Brillouin zone (solid black lines) and weaker replicas at the Γ points of the CDW-folded Brillouin zones [demonstrated by green dashed lines in Figs. 4(a) and 4(c)].

The electronic structure at higher binding energies indicates that a CDW deformation persists in the hidden state, even though the gaps are suppressed. In Figs. 4(c) and 4(d), we compare intensity maps at a binding energy of 300 meV in a metallic region [Fig. 4(c)] and an insulating region [Fig. 4(d)]. Both datasets exhibit a chiral pattern attributed to mirror symmetry breaking caused by the formation of Star of David clusters [27]. We emphasize that no measurable differences were observed in the insulating regions before and after the current pulse (see Fig. S1 in the Supplemental Material [43]). Throughout the text, we refer to the band structure of 1*T*-TaS_2 as chiral, in accordance with the accepted notation in the field. However, it is important to note that 1*T*-TaS_2 is centrosymmetric, and therefore not chiral in the crystallographic sense. Instead, it is more accurately described as *pseudochiral*, a state characterized by the absence of mirror symmetry in the bulk three-dimensional (3D) band structure [44].

The two possible configurations of the BZ in the CCDW phase are illustrated in Fig. 4(e). Remarkably, our results indicate that the resulting Fermi surface of the hidden state also breaks mirror symmetry, seemingly inheriting its chirality from the underlying CDW domains.

Moreover, by comparing the chiral patterns at the same metallic point both in the hidden state and prior to the application of the current pulse, we show that the chirality remains unchanged by the current pulse (see Fig. S2 [43]). This evidence, shown in the Supplemental Material [43], strongly suggests that the transition into the hidden state does not involve a complete melting of the CDW. This conclusion is

in agreement with the evident uniform chirality of domains observed in real-space STM data [4].

The data from the metallic parts, both the dispersion and the Fermi surface, closely resemble those of the NCCDW state [45]. However, STM measurements reveal that in the hidden phase, the CCDW is fragmented into a disordered network of domains, each approximately tens of nanometers in size [4]. This domain configuration is distinct from that observed in the NCCDW state. The spot size used in our experiment covers approximately 1000 domains. Given that the domain walls are around $\sim$1 Å in width [24], their contribution to the ARPES spectra is negligible. Combined with the distinct chirality of the Fermi surface we find (see Fig. S3 [43]) this confirms that the metallic nature of the hidden state is not due to conducting domain walls.

E. Out of plane dispersion measurements

After confirming that the CDW persists in both the metallic and insulating regions of the sample following the current pulse, we turn our attention to understanding the differences between these regions. In Fig. 5, we present photon energy dependent data measured at representative points in both areas. The out of plane dispersion was recorded at a fixed parallel momentum, $k_{\parallel} = -0.66\,\text{Å}^{-1}$ [indicated by the red dot in the inset of Fig. 5(d)]. This point lies near the center of the reconstructed Brillouin zone, Γ', as seen by the faint replica of the band at a binding energy of $\sim$1.25 eV.

Figures 5(a) and 5(b) correspond to an insulating region while Figs. 5(c) and 5(d) are from a metallic region. Figures 5(a) and 5(c) show data along Γ-M measured using 77 eV photons. The white dashed lines represent the in-plane momentum at which the dispersion out of plane was measured. In Figs. 5(b) and 5(d) we show a color plot combining the EDCs at different k_z values.

The k_z dispersion of the two uppermost subbands formed by the CCDW, extracted by tracking the maxima in the EDCs, is shown in Figs. 5(e) and 5(f). The bandwidths of the two bands are approximately 100 and 50 meV, respectively. Notably, both bands show a clear doubling of the expected periodicity, indicating a doubling of the unit cell. This observation is consistent with a charge density wave out of plane with two unit cell periodicity or a dimerization of pairs of Star of David clusters on two neighboring planes. The CDW replicas exhibit significantly weaker intensity compared to the main band. The double periodicity becomes more pronounced when the dispersion is measured at the Γ' point instead of the Γ point. The dashed white line in Fig. 5(b) represents the results of a DFT calculation for an alternating stacking AL configuration, where two vertically aligned Star of David clusters form pairs within each bilayer, and these pairs are shifted relative to the pairs in neighboring bilayers [36]. Our results show qualitative agreement with the DFT calculation. Previous studies were somewhat inconclusive on this point [46,47]. The difference could be related to the significantly smaller light spot used in our study.

When examining the k_z dispersion in the metallic regions, we observe a different behavior. In Figs. 5(c) and 5(d), we present data along Γ-M measured using 77 eV photons, and photon energy dependence of the EDCs measured in a metallic part of the sample, respectively. The extracted dispersion is shown in Fig. 5(g), revealing only one band at this $k_{\parallel}$ value. The bandwidth is approximately 200 meV, which is significantly larger than that observed in the insulating region. Notably, we do not find the double periodicity; instead, the dispersion is in agreement with the atomic-lattice unit cell.

III. DISCUSSION

Our study reveals that the hidden state in 1T-TaS_2 hosts a holelike band crossing the Fermi level, resulting in a Fermi surface reminiscent of the nearly commensurate NCCDW phase. This similarity is not surprising, given the structural resemblance between the two phases, both characterized by domains of commensurate CDW order. However, the mechanisms underlying the metallicity of these phases remain elusive. While it has been proposed that conducting domain-wall regions, where the CDW order parameter $\Delta = 0$, form channels that contribute to the overall conductivity, our ARPES measurements suggest that this mechanism alone cannot account for the observed metallic behavior. Although such channels may be locally conductive, they are insufficient to explain the emergence of a robust Fermi surface and substantial spectral weight at the Fermi level.

We show that the hidden Fermi surface exhibits distinct chirality arising from the CCDW domain arrangements, an intrinsic property of the domains themselves rather than the domain walls. Furthermore, the significant spectral weight observed in ARPES, which is surface sensitive, indicates that each domain is intrinsically metallic, and the contribution from domain walls is minimal. Importantly, the in-plane CDW motif remains essentially intact across both insulating and metallic regions, suggesting that the metallicity does not result from CDW melting or disordering, but from a more subtle structural transformation.

Our findings establish a compelling link between the stacking configuration of 1T-TaS_2 and its emergent electronic properties. While the monolayer is likely a Mott insulator [37], in the bulk, first-principles calculations have shown that the out of plane stacking of Star of David clusters plays a decisive role in shaping the in-plane electronic dispersion, modulating gap structures and bandwidths depending on the stacking configuration [34,36]. Specifically, DFT calculations by Lee *et al.* [34] indicate that the AL-stacking configuration, in which vertical dimers of Star of David clusters are stacked such that the central atom of one dimer aligns with one of the outer atoms of a neighboring cluster, is energetically the most favorable. The L stacking, where there are no dimers, has only a slightly higher energy. This small energy difference suggests that a stacking rearrangement from AL to L can be induced by a moderate external perturbation such as a current pulse.

To uncover the nature of this transformation, we examined the out of plane band dispersion at binding energies where differences between metallic and insulating regions are minimized, isolating the influence of interlayer effects. In the insulating regions, the k_z dispersion shows a doubled periodicity and reduced bandwidth, consistent with interlayer dimerization and a doubling of the unit cell along the c axis,

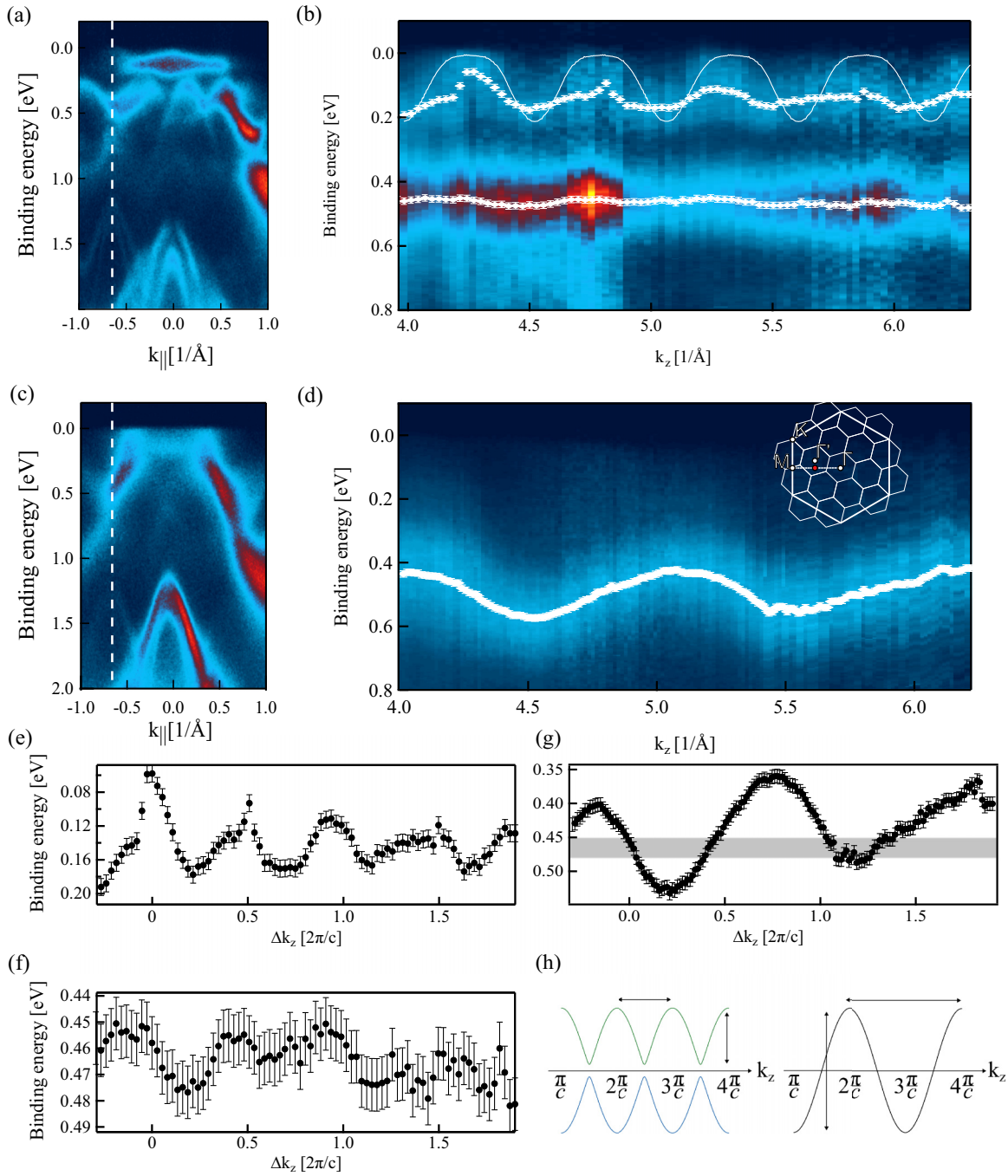

FIG. 5. Out of plane dispersion. (a) ARPES image along the Γ-*M* direction from an insulating region measured with 77 eV photons. The white dotted line marks $k_{\|}$ where the photon energy scan was measured. (b) Intensity as a function of binding energy and k_z for photon energies between 48 and 140 eV. White diamonds indicate the binding energy of the spectral peak at each k_z, extracted from fits to the EDCs; error bars correspond to the larger of the fit uncertainty and the experimental energy resolution (10 meV). The dashed white line represents the calculated out of plane dispersion in the AL-stacking configuration from Ref. [36]. Each EDC is normalized by the intensity at the peak at low binding energies. The dispersion of the two bands exhibits a periodicity that is double the expected value based on the atomic unit cell size. (c),(d) Same as (a,b) measured in a metallic region. Here, the dispersion periodicity follows the atomic BZ. Inset: the red dot marks the location in $k_{\|}$ at which the k_z data were measured. It is close to the Γ′ point. (e),(f) The k_z dispersion of the flat band and the second valance band, respectively, as extracted from panel (b). (g) The k_z dispersion of the topmost band in the metallic region as extracted from (c). The shaded gray area represents the bandwidth of the band shown in (f). (h) Schematic illustration of the k_z dispersion. The right side shows the dispersion of a band with one electron per unit cell. The left side shows the dispersion when the unit cell is doubled, either due to dimerization or a two-unit cell CDW.

as previously reported [35] [see Fig. 1(b)]. The dashed white line in Fig. 5(b) shows the calculated out of plane dispersion for the AL-stacking configuration, which matches well with our data from the insulating regions.

In contrast, the metallic regions exhibit a single-period k_z dispersion closely matching the primitive lattice periodicity and a broader bandwidth, indicating the absence of dimerization [see Fig. 1(b)]. These observations suggest that the current pulse disrupts the out of plane configuration, breaking the interlayer correlations that stabilize the insulating state. The new configuration restores a simpler stacking periodicity and enables coherent interlayer hopping, thereby giving rise to a three-dimensional metallic state.

This hidden metallic phase represents an unusual electronic structure among transition metal dichalcogenides: the out of plane (interlayer) bandwidth exceeds the in-plane bandwidth. This is in agreement with transport measurements showing that the resistivity anisotropy in the NCCDW state is close to 1 [48].

Such an inversion of dimensionality, where transport and electronic coherence are dominated by the out of plane direction, challenges conventional views of quasi-two-dimensional (2D) physics and may open new avenues for engineering anisotropic transport and manipulating quantum phases in layered materials.

ACKNOWLEDGMENTS

We thank Assa Auerbach and Daniel Podolsky for useful discussions. We acknowledge Diamond Light Source for time on Beamline i05 under Proposal No. SI33131. We acknowledge SOLEIL for provision of synchrotron radiation facilities under Proposal No. 20230771 and we would like to thank Chiara Bigi and Francois Bertran for assistance in using beamline CASSIOPEE. The work at the Technion was supported by Israeli Science Foundation Grant No. ISF-568/25.

A.K. conceived the experiment. I.F. prepared the 1*T*-TaS2 single crystals. Y.N. performed the ARPES experiments and analyzed the ARPES data. R.A.G.K, I.M., A.D., N.R., S.K.P., and Y.J. performed ARPES measurements. A.L., M.D.W., and C.C. provided support at the synchrotron beamline. Y.N. and A.K. wrote the manuscript with contributions from all authors.

The authors declare that they have no competing interests.

DATA AVAILABILITY

The data that support the findings of this article are not publicly available upon publication because it is not technically feasible and/or the cost of preparing, depositing, and hosting the data would be prohibitive within the terms of this research project. The data are available from the authors upon reasonable request.

[1] H. Oike, M. Kamitani, Y. Tokura, and F. Kagawa, Kinetic approach to superconductivity hidden behind a competing order, Sci. Adv. **4**, eaau3489 (2018).

[2] T.-R. T. Han, F. Zhou, C. D. Malliakas, P. M. Duxbury, S. D. Mahanti, M. G. Kanatzidis, and C.-Y. Ruan, Exploration of metastability and hidden phases in correlated electron crystals visualized by femtosecond optical doping and electron crystallography, Sci. Adv. **1**, e1400173 (2015).

[3] I. Madan, J. Buh, V. V. Baranov, V. V. Kabanov, A. Mrzel, and D. Mihailovic, Nonequilibrium optical control of dynamical states in superconducting nanowire circuits, Sci. Adv. **4**, eaao0043 (2018).

[4] Y. A. Gerasimenko, P. Karpov, I. Vaskivskyi, S. Brazovskii, and D. Mihailovic, Intertwined chiral charge orders and topological stabilization of the light-induced state of a prototypical transition metal dichalcogenide, npj Quantum Mater. **4**, 32 (2019).

[5] T. Frigge, B. Hafke, T. Witte, B. Krenzer, C. Streubühr, A. Samad Syed, V. Mikšić Trontl, I. Avigo, P. Zhou, M. Ligges, D. von der Linde, U. Bovensiepen, M. Horn-von Hoegen, S. Wippermann, A. Lücke, S. Sanna, U. Gerstmann, and W. G. Schmidt, Optically excited structural transition in atomic wires on surfaces at the quantum limit, Nature (London) **544**, 207 (2017).

[6] F. Di Salvo, B. Bagley, J. Voorhoeve, and J. Waszczak, Preparation and properties of a new polytype of tantalum disulfide (4Hb-TaS_2), J. Phys. Chem. Solids **34**, 1357 (1973).

[7] S. H. Sung, N. Schnitzer, S. Novakov, I. El Baggari, X. Luo, J. Gim, N. M. Vu, Z. Li, T. H. Brintlinger, Y. Liu, W. Lu, Y. Sun, P. B. Deotare, K. Sun, L. Zhao, L. F. Kourkoutis, J. T. Heron, and R. Hovden, Two-dimensional charge order stabilized in clean polytype heterostructures, Nat. Commun. **13**, 413 (2022).

[8] M. Budden, T. Gebert, M. Buzzi, G. Jotzu, E. Wang, T. Matsuyama, G. Meier, Y. Laplace, D. Pontiroli, M. Riccò, F. Schlawin, D. Jaksch, and A. Cavalleri, Evidence for metastable photo-induced superconductivity in K_3C_{60}, Nat. Phys. **17**, 611 (2021).

[9] J. Zhang, X. Tan, M. Liu, S. W. Teitelbaum, K. W. Post, F. Jin, K. A. Nelson, D. N. Basov, W. Wu, and R. D. Averitt, Cooperative photoinduced metastable phase control in strained manganite films, Nat. Mater. **15**, 956 (2016).

[10] A. Zong, X. Shen, A. Kogar, L. Ye, C. Marks, D. Chowdhury, T. Rohwer, B. Freelon, S. Weathersby, R. Li, J. Yang, J. Checkelsky, X. Wang, and N. Gedik, Ultrafast manipulation of mirror domain Walls in a charge density wave, Sci. Adv. **4**, eaau5501 (2018).

[11] A. de la Torre, D. M. Kennes, M. Claassen, S. Gerber, J. W. McIver, and M. A. Sentef, Colloquium: Nonthermal pathways to ultrafast control in quantum materials, Rev. Mod. Phys. **93**, 041002 (2021).

[12] X. Shi, W. You, Y. Zhang, Z. Tao, P. M. Oppeneer, X. Wu, R. Thomale, K. Rossnagel, M. Bauer, H. Kapteyn, and M. Murnane, Ultrafast electron calorimetry uncovers a new long-lived metastable state in 1*T*-$TaSe_2$ mediated by mode-selective electron-phonon coupling, Sci. Adv. **5**, eaav4449 (2019).

[13] L. Stojchevska, I. Vaskivskyi, T. Mertelj, P. Kusar, D. Svetin, S. Brazovskii, and D. Mihailovic, Ultrafast switching to a stable hidden quantum state in an electronic crystal, Science **344**, 177 (2014).

[14] L. Ma, C. Ye, Y. Yu, X. F. Lu, X. Niu, S. Kim, D. Feng, D. Tománek, Y.-W. Son, X. H. Chen, and Y. Zhang, A metallic mosaic phase and the origin of Mott-insulating state in 1*T*-TaS_2, Nat. Commun. **7**, 10956 (2016).

[15] I. Vaskivskyi, I. A. Mihailovic, S. Brazovskii, J. Gospodaric, T. Mertelj, D. Svetin, P. Sutar, and D. Mihailovic, Fast electronic resistance switching involving hidden charge density wave states, Nat. Commun. **7**, 11442 (2016).

[16] R. Venturini, A. Mraz, I. Vaskivskyi, Y. Vaskivskyi, D. Svetin, T. Mertelj, L. Pavlovič, J. Cheng, G. Chen, P. Amarasinghe, S. B. Qadri, S. B. Trivedi, R. Sobolewski, and D. Mihailovic, Ultraefficient resistance switching between charge ordered phases in $1T$-TaS_2 with a single picosecond electrical pulse, Appl. Phys. Lett. **120**, 253510 (2022).

[17] I. Vaskivskyi, J. Gospodaric, S. Brazovskii, D. Svetin, P. Sutar, E. Goreshnik, I. A. Mihailovic, T. Mertelj, and D. Mihailovic, Controlling the metal-to-insulator relaxation of the metastable hidden quantum state in $1T$-TaS_2, Sci. Adv. **1**, e1500168 (2015).

[18] J. Maklar, J. Sarkar, S. Dong, Y. A. Gerasimenko, T. Pincelli, S. Beaulieu, P. S. Kirchmann, J. A. Sobota, S. Yang, D. Leuenberger, R. G. Moore, Z.-X. Shen, M. Wolf, D. Mihailovic, R. Ernstorfer, and L. Rettig, Coherent light control of a metastable hidden state, Sci. Adv. **9**, eadi4661 (2023).

[19] I. Vaskivskyi, A. Mraz, R. Venturini, G. Jecl, Y. Vaskivskyi, R. Mincigrucci, L. Foglia, D. De Angelis, J.-S. Pelli-Cresi, E. Paltanin, D. Fainozzi, F. Bencivenga, C. Masciovecchio, and D. Mihailovic, A high-efficiency programmable modulator for extreme ultraviolet light with nanometre feature size based on an electronic phase transition, Nat. Photonics **18**, 458 (2024).

[20] D. Mihailovic, D. Svetin, I. Vaskivskyi, R. Venturini, B. Lipovšek, and A. Mraz, Ultrafast non-thermal and thermal switching in charge configuration memory devices based on $1T$-TaS_2, Appl. Phys. Lett. **119**, 013106 (2021).

[21] A. Mraz, R. Venturini, D. Svetin, V. Sever, I. A. Mihailovic, I. Vaskivskyi, B. Ambrozic, G. Dražić, M. D'Antuono, D. Stornaiuolo, F. Tafuri, D. Kazazis, J. Ravnik, Y. Ekinci, and D. Mihailovic, Charge configuration memory devices: Energy efficiency and switching speed, Nano Lett. **22**, 4814 (2022).

[22] S. C. Bayliss, A. M. Ghorayeb, and D. R. P. Guy, Thermal and transport evidence for a phase transition in $1T$-TaS_2 observed at 282 K upon warming, J. Phys. C **17**, L533 (1984).

[23] K. Rossnagel, On the origin of charge-density waves in select layered transition-metal dichalcogenides, J. Phys.: Condens. Matter **23**, 213001 (2011).

[24] X. L. Wu and C. M. Lieber, Hexagonal domain-like charge density wave phase of TaS_2 determined by scanning tunneling microscopy, Science **243**, 1703 (1989).

[25] R. E. Thomson, B. Burk, A. Zettl, and J. Clarke, Scanning tunneling microscopy of the charge-density-wave structure in $1T$-TaS_2, Phys. Rev. B **49**, 16899 (1994).

[26] X. L. Wu and C. M. Lieber, Direct observation of growth and melting of the hexagonal-domain charge-density-wave phase in $1T$-TaS_2 by scanning tunneling microscopy, Phys. Rev. Lett. **64**, 1150 (1990).

[27] H. F. Yang, K. Y. He, J. Koo, S. W. Shen, S. H. Zhang, G. Liu, Y. Z. Liu, C. Chen, A. J. Liang, K. Huang, M. X. Wang, J. J. Gao, X. Luo, L. X. Yang, J. P. Liu, Y. P. Sun, S. C. Yan, B. H. Yan, Y. L. Chen, X. Xi, and Z. K. Liu, Visualization of chiral electronic structure and anomalous optical response in a material with chiral charge density waves, Phys. Rev. Lett. **129**, 156401 (2022).

[28] G. Liu, T. Qiu, K. He, Y. Liu, D. Lin, Z. Ma, Z. Huang, W. Tang, J. Xu, K. Watanabe, T. Taniguchi, L. Gao, J. Wen, J.-M. Liu, B. Yan, and X. Xi, Electrical switching of ferro-rotational order in nanometre-thick $1T$-TaS_2 crystals, Nat. Nanotechnol. **18**, 854 (2023).

[29] E. Tosatti and P. Fazekas, On the nature of the low-temperature phase of $1T$-TaS_2, J. Phys., Colloq. **37**, C4-165 (1976).

[30] K. T. Law and P. A. Lee, $1T$-TaS_2 as a quantum spin liquid, Proc. Natl. Acad. Sci. USA **114**, 6996 (2017).

[31] Z. Wu, K. Bu, W. Zhang, Y. Fei, Y. Zheng, J. Gao, X. Luo, Z. Liu, Y.-P. Sun, and Y. Yin, Effect of stacking order on the electronic state of $1T$-TaS_2, Phys. Rev. B **105**, 035109 (2022).

[32] P. Fazekas and E. Tosatti, Charge carrier localization in pure and doped $1T$-TaS_2, Phys. B+C **99**, 183 (1980).

[33] C. J. Butler, M. Yoshida, T. Hanaguri, and Y. Iwasa, Mottness versus unit-cell doubling as the driver of the insulating state in $1T$-TaS_2, Nat. Commun. **11**, 2477 (2020).

[34] S.-H. Lee, J. S. Goh, and D. Cho, Origin of the insulating phase and first-order metal-insulator transition in $1T$-TaS_2, Phys. Rev. Lett. **122**, 106404 (2019).

[35] Q. Stahl, M. Kusch, F. Heinsch, G. Garbarino, N. Kretzschmar, K. Hanff, K. Rossnagel, J. Geck, and T. Ritschel, Collapse of layer dimerization in the photo-induced hidden state of $1T$-TaS_2, Nat. Commun. **11**, 1247 (2020).

[36] T. Ritschel, H. Berger, and J. Geck, Stacking-driven gap formation in layered $1T$-TaS_2, Phys. Rev. B **98**, 195134 (2018).

[37] V. Vaňo, M. Amini, S. C. Ganguli, G. Chen, J. L. Lado, S. Kezilebieke, and P. Liljeroth, Artificial heavy fermions in a van der Waals heterostructure, Nature (London) **599**, 582 (2021).

[38] A. Ribak, I. Silber, C. Baines, K. Chashka, Z. Salman, Y. Dagan, and A. Kanigel, Gapless excitations in the ground state of $1T$-TaS_2, Phys. Rev. B **96**, 195131 (2017).

[39] A. Damascelli, Probing the electronic structure of complex systems by ARPES, Phys. Scr. **T109**, 61 (2004).

[40] T. R. Devidas, D. Yahav, J. T. Reichanadter, S. C. Haley, M. Sterenberg, J. E. Moore, J. B. Neaton, J. G. Analytis, B. Kalisky, and E. Maniv, Dark metastable conduction channels near a metal-insulator transition, arXiv:2405.02036.

[41] T. Pillo, J. Hayoz, H. Berger, M. Grioni, L. Schlapbach, and P. Aebi, Remnant fermi surface in the presence of an underlying instability in layered $1T$-TaS_2, Phys. Rev. Lett. **83**, 3494 (1999).

[42] C. Sohrt, A. Stange, M. Bauer, and K. Rossnagel, How fast can a Peierls–Mott insulator be melted? Faraday Discuss. **171**, 243 (2014).

[43] See Supplemental Material at http://link.aps.org/supplemental/10.1103/kj9t-8mys for insulating spectra comparison, additional polar and spatial maps, NCCDW ARPES data and spot size calibration, which includes Ref. [39].

[44] A. Louat, M. D. Watson, T. K. Kim, D. Ni, R. J. Cava, and C. Cacho, The pseudochiral Fermi surface of α-RuI_3, Commun. Phys. **7**, 43 (2024).

[45] E. Lahoud, O. N. Meetei, K. B. Chaska, A. Kanigel, and N. Trivedi, Emergence of a novel pseudogap metallic state in a disordered 2D mott insulator, Phys. Rev. Lett. **112**, 206402 (2014).

[46] A. S. Ngankeu, S. K. Mahatha, K. Guilloy, M. Bianchi, C. E. Sanders, K. Hanff, K. Rossnagel, J. A. Miwa, C. Breth Nielsen, M. Bremholm, and P. Hofmann, Quasi-one-dimensional

metallic band dispersion in the commensurate charge density wave of $1T$-TaS_2, Phys. Rev. B **96**, 195147 (2017).

[47] J. Jung, J. W. Park, J. Kim, and H. W. Yeom, Surface enhanced electron correlation on the trivial quasi-two-dimensional bulk insulator $1T$-TaS_2, Phys. Rev. B **106**, 155406 (2022).

[48] E. Martino, A. Pisoni, L. Ćirić, A. Arakcheeva, H. Berger, A. Akrap, C. Putzke, P. J. W. Moll, I. Batistić, E. Tutiš, L. Forró, and K. Semeniuk, Preferential out-of-plane conduction and quasi-one-dimensional electronic states in layered $1T$-TaS_2, npj 2D Mater. Appl. **4**, 7 (2020).